AI-GUIDED CLOSED-LOOP DISCOVERY OF HARD MULTIPLE PRINCIPAL ELEMENT ALLOYS

Anonymous authors
Paper under double-blind review

ABSTRACT

Multi-principal element alloys (MPEAs) form a unique class of alloys (3 or more elements) that are sought-after due to their exceptional mechanical properties. However, a significant challenge in the discovery and design of MPEAs lies in the vast and complex compositional space they occupy, which is both high-dimensional and sparsely explored. Traditional methods for identifying MPEAs with desirable properties tend to rely heavily on trial-and-error experimentation, which is time-consuming and inefficient. In this work, we apply an active learning approach, PAL 2.0, utilizing a Bayesian optimization framework as a means to significantly accelerate the discovery of MPEAs with particularly high hardness. The framework closely integrates physics-based Gaussian process models with experimental validation. Our methodology enables the model to intelligently navigate the compositional space and make informed decisions about the most promising alloys to synthesize and test. Based on recommendations made by PAL 2.0, we successfully synthesized 20 new MPEAs through a rapid arc-melting process.Gienger et al. (2024) Among these 20, we identified two new alloys with exceptionally high Vickers hardness values of 1269 and 1263. While the original training dataset had only three MPEAs with hardness above 1000, our method recognized five additional compositions with a hardness over 1000, thereby doubling the number of very hard MPEAs. The most striking discovery is the appearance of silicon and tantalum together in the alloys, an "out of distribution" combination not seen in any high hardness alloy within the original training dataset. This study demonstrates the power of PAL 2.0 as a fast, efficient, and scalable tool for the discovery of materials with optimal properties. It offers a pathway to explore other complex, high-dimensional material spaces, paving the way for creative advancements in materials science.

1 INTRODUCTION

The development of advanced materials with exceptional mechanical properties is critical to various engineering applications, ranging from aerospace to power generation. In recent years, MPEAs, and the closely related class of materials known as high-entropy alloys (HEAs), have emerged as a promising class of materials that challenge traditional alloy design strategies. Unlike conventional alloys, which consist of a single principal element, MPEAs are composed of three or more elements in near-equiatomic concentrations (Yeh et al. (2004); Ostovari Moghaddam et al. (2021)). This alloying approach allows researchers to exploit a vastly expanded compositional space, leading to the discovery of alloys with remarkable properties, including high strength, ductility, and thermal stability (George et al. (2020)). One of the most intriguing features of MPEAs is their ability to maintain a stable solid-solution phase. This phenomenon, theoretically driven by configurational entropy, inhibits the formation of brittle intermetallic phases and promotes the formation of complex microstructures that can be tuned for desired mechanical properties. Consequently, MPEAs have shown potential for applications in extreme loading and temperature environments. However, despite their promise, the vast compositional design space of MPEAs makes it challenging to systematically identify alloy compositions that exhibit optimal mechanical properties using "Edisonian" materials discovery approaches (Liu et al. (2022)). This situation is tailor-made for the intervention of machine learning and high-throughput approaches to navigate the MPEA design space more effectively and efficiently.

Computational and experimental methods employed in MPEA design New experimental approaches have emerged to accelerate the discovery of MPEAs. These include high-throughput experimentation (Bresnahan & Poerschke (2024); Koneru et al. (2022); Gienger et al. (2024); Hastings et al. (2025)), additive manufacturing (Li et al. (2022); Pegues et al. (2021)), and combinatorial development (Rao et al. (2022a)). Following manufacturing, Vickers microhardness tests are frequently conducted as a practical proxy for mechanical strength in high-throughput workflows since hardness is relatively easy to measure on small ingots, and correlates reasonably well with strength, making it an ideal screening target (Paramore et al. (2025); Roy et al. (2023); Acemi et al. (2024)). However, purely experimental methods can be rather expensive in terms of labor and resources.

As an alternative to experimental studies, several computational methods, such as the well-known and well-used CALculation of PHAse Diagrams (CALPHAD) and density functional theory (DFT), offer a calculation-based approach to materials discovery (Rao et al. (2019); Huang et al. (2018); Körmann et al. (2015); Wang et al. (2019)). Computational frameworks like CALPHAD and DFT, while powerful, are often computationally intensive for composition selection, deterring optimization across vast multi-principal element alloy design spaces. To address these shortcomings, a range of supervised and generative machine learning (ML) techniques have been developed to accelerate alloy discovery by predicting phase stability, mechanical properties, and processing windows. For example, Chandraker *et al.* (Chandraker et al. (2025)) trained a series of ML models to predict the yield strength of the Co-Cr-Fe-Mn-Ni alloy system given composition, printing parameters and testing conditions as inputs and in Ref. 39 authors use ML models to predict room temperature fatigue life in single-phase Co-Cr-Fe-Mn-Ni system and the multi-phase Al-Co-Cr-Fe-Ni system. The success of these methods shows the power of ML approaches to predict the behavior of HEAs.

In addtion to generative modeling, active learning strategies such as Bayesian optimization have gained significant traction in designing new materials (Sharma Priyadarshini et al. (2024); Halpren et al. (2024); Sulley et al. (2024); Kusne et al. (2020); Liu et al. (2022); Li et al. (2024); Roy et al. (2023); Rao et al. (2022b)). Constraint-aware and supply-chain-informed Bayesian design frameworks have been used to optimize alloys (Khatamsaz et al. (2023); Mulukutla et al. (2025)), while others have implemented batch Bayesian optimization to efficiently identify alloys maximizing specific hardness and stiffness (Paramore et al. (2025)). A primary focus of the studies mentioned above has been on multi-objective optimization for a given alloy system such as FeCrNiCoCu.

"Closed loop" materials discovery Although *in silico* materials discovery and modeling has several benefits, the ultimate goal remains to translate the discovery to synthesizable materials. To achieve this, closed-loop and active learning approaches are being adopted. These approaches involve iterative cycles of experimental testing that are used to inform and improve predictions of better materials based on computational models (Kusne et al. (2020)). Optimal materials identified by a model are manufactured and tested, and the experimental data are fed back to the model to inform further predictions (Alvi et al. (2025); Angello et al. (2024)). For instance, studies have used multi-task and deep Gaussian process Bayesian optimization to leverage property correlations in multi-objective optimization of FCC HEAs (Alvi et al. (2025)). Closed-loop frameworks have been found to reduce the overall time for materials discovery by over 90% (Kavalsky et al. (2023)), and they have shown success in the discovery of organic solid-state lasers (Strieth-Kalthoff et al. (2024)) and functional inorganic compounds (Kusne et al. (2020)), MPEAs (Rao et al. (2022b)) and superconductors (Pogue et al. (2023)).

In this study, we identified novel high-hardness MPEA compositions building on our previously developed materials discovery framework, PAL 2.0 (Sharma Priyadarshini et al. (2024)). We employ Bayesian optimization with a physics-based prior, allowing it to accurately predict a target material property based on known physio-chemical properties of the constituent elements. Here, we show that using PAL 2.0 inside a closed loop, with rapid synthesis and characterization, enabled quick and efficient exploration of the large compositional space of MPEAs, yielding alloys of significantly higher hardness within only three cycles. The hardness values of these alloys exceed those discovered by Roy *et al.* using their GAN model (Roy et al. (2023)), indicating that PAL 2.0 can outperform generative models for MPEA discovery.

2 METHODS AND MATERIALS

2.1 PHYSICAL ANALYTICS PIPELINE (PAL) 2.0

PAL 2.0 is a materials discovery method that uses Bayesian optimization in conjunction with a physics-based surrogate model (Sharma Priyadarshini et al. (2024)). The strength of the method lies in the combination of feature engineering based on decision trees, a neural network prior, and a Gaussian process surrogate model. The objective of materials discovery algorithms is to optimize a given material property, $f(x_D)$, where x_D are the input descriptors used to describe the search space. The inputs, x_D, are usually physico-chemical properties or "one-hot-encoded" composition vectors. The first task to address is to identify the search-space representation, x_D. In PAL 2.0, we use XGBoost (Chen & Guestrin (2016)) to select elemental physico-chemical properties that are put together as an input vector, x_D. Details of our choice of XGBoost over other feature engineering methods can be found in Ref. 40.

Second, we construct a surrogate model that approximates $f(x_D)$. Here, we consider the surrogate model to be a Gaussian process (GP) with a prior mean function $m(x_D)$, and a covariance function, $k(x_D, x'_D)$. The posterior probability distribution on the mean function (μ^i) and covariance (v^i) of the GP model is evaluated based on new observations ($x_D^{(t)}$) and the prior using the following equations,

$$\mu^i = m(x_D) + k(x_D, x_D^{(t)})(k(x_D, x_D^{(t)}) + \eta^2 I)^{-1}(y(x_D) - m(x_D)), \quad (1)$$

$$v^i = k(x_D^{(t)}, x_D^{(t)}) - k(x_D, x_D^{(t)})(k(x_D, x_D^{(t)}) + \eta^2 I)^{-1} k(x_D, x_D^{(t)})^T. \quad (2)$$

We use two choices for $m(x_D)$. The first is setting $m(x_D) = 0$, which is a GP model with a zero-mean for the prior. Our second choice is representing $m(x_D)$ using a small neural network (NN) as described in Ref. 40. The covariance function $k(x_D, x'_D)$ gives a measure of the similarity between two candidates in terms of their physical descriptors (D). In PAL 2.0, we measure this similarity using a 5/2 Matérn kernel. The hyperparameters of our models (for the mean function and covariance) are optimized using a "maximum likelihood estimate" approach (for (2014)) in concert with the Adam optimizer (Kingma & Ba (2014)). We implement the commonly used "Expected Improvement" (EI) acquisition function (Snoek et al. (2012)) to determine the next set of promising material candidates. We have found EI to work well in the past for our studies of metal halide perovskite systems (Herbol et al. (2018; 2020); Sharma Priyadarshini et al. (2024)).

Finally, we run PAL 2.0 with two Gaussian Process models ($m(x_D)$=0 and $m(x_D)$ given by a NN) to obtain alloy candidates for manufacturing. The final candidates are chosen based on a consensus of recommendations made by the two GP models. This is accomplished by making recommendations using both GP-0 and GP-NN in the Bayesian optimization framework. The recommendations are then compared and only common recommendations from both surrogate models are selected for subsequent manufacturing. The PAL 2.0 codebase is implemented using PyTorch's Bayesian optimization library (BOTorch) (Balandat et al. (2019)). Figure 1 shows a schematic of the workflow for a computational-experimental closed-loop discovery approach that uses PAL 2.0. In this paper, we focus on using only the PAL 2.0 framework to provide recommendations for manufacturing and do not compare the performance of PAL 2.0 against other methods since experiments are part of the loop here. We have previously benchmarked the performance of PAL 2.0 against several state-of-the-art materials discovery algorithms in Ref. 40. We refer interested readers to this previous publication for further benchmarking details.

2.2 CLUSTERING USING k-MEANS TO GENERATE NOVEL ALLOY COMPOSITIONS

To expand the search space of the closed-loop experiments beyond the dataset provided in Ref. 8, we developed an algorithm to generate novel alloy compositions based on existing MPEAs. Initially, k-means clustering is performed on a dataset of approximately 350 experimentally confirmed MPEAs with known hardness values (Borg et al. (2020)). The algorithm then generates new alloy compositions based on the cluster centroids with some random variation.

We calculate two metrics to determine the optimal number of clusters for the k means clustering method. These are the inertia and silhouette scores. Inertia measures the distance of each point in a cluster from that cluster's centroid, and it is calculated using Eqn. equation 3. I is the overall inertia

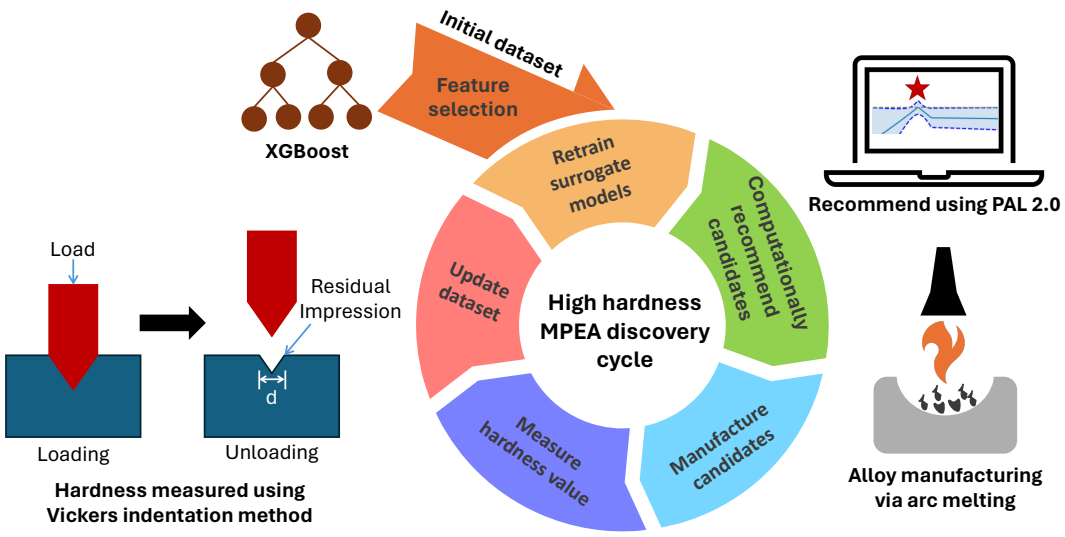

Figure 1: Schematic showing the workflow for closed-loop materials discovery methodology using PAL 2.0 and the arc-melting facility at the Johns Hopkins University Applied Physics Laboratory (JHU/APL).

of the dataset, n is the total number of data points, x_i is the position of a point, and μ_i is the position of the centroid of the cluster to which point i belongs.

$$I = \sum_{i=1}^{n} (x_i - \mu_i)^2. \tag{3}$$

Values for the inertia for each number of clusters (k) are shown in Fig. 6a in the Appendix. Generally, the optimal value of k is located near the "elbow" of the inertia plot, as this offers a compromise between cluster compactness and model simplicity. Our results suggest k values of 2, 3, or 4 to be appropriate. We use the silhouette score as a second metric to determine the optimal number of clusters. A silhouette score is calculated for a single data point using the following equation,

$$S(i) = \frac{b(i) - a(i)}{\max\{a(i), b(i)\}}. \tag{4}$$

Here, $S(i)$ is the silhouette coefficient of the data point i, $a(i)$ is the average distance between i and all the other data points in the cluster to which i belongs, and $b(i)$ is the average distance from i to all clusters to which i does not belong. It essentially measures the distance of each point from its assigned cluster in contrast to its distance from all other clusters. These scores range from -1 to 1. High silhouette scores are desirable, as they indicate high separation between clusters. Figure 6b shows that 2 clusters result in the maximum mean silhouette score (0.37), which is significantly higher than the scores for 3 and 4 clusters (0.28). Furthermore, Fig. 7 shows that two clusters result in the most even distribution of scores and the fewest number of negative scores. Based on these results from the inertia and silhouette analyses, we chose two as the number of clusters and used these clusters to generate novel MPEA compositions to expand PAL 2.0's search-space.

2.3 Experimental Set up and Manufacturing

Candidate alloy recommendations from PAL 2.0 were manufactured in the arc-melting facility at JHU/APL using the procedure described in Ref. Gienger et al. (2024). We weigh elemental feedstock in accordance with PAL 2.0's recommendations and place them in arc-melting sample hearths. The target sample weight is set to 1 gram for the final composition. We arc-melted the samples using a MRF SA-200 arc-melt furnace with currents up to 120 A in an argon atmosphere. Each sample is melted two times, flipped, and then melted once or twice more to encourage homogeneity. To account for volatilization and in order to end with a composition closer to the predicted material,

samples containing manganese, chromium or aluminum were made with initial feedstock weights $\sim$10 wt% higher than the final target weights. In our experiments and characterization, we only included samples where the post-melt mass matched the pre-melt mass, indicating minimal material loss during arc-melting. This was done to mitigate the risk of high compositional uncertainties arising in arc-melted alloys that contain elements with significantly different melting and boiling points.

The arc-melted samples are sectioned and cold-mounted in epoxy, with up to three samples in one mount for expediency of preparation and hardness testing. The samples were prepared under standard metallographic procedures down to 1200 grit, followed by a 1 μm alumina polish and finished with 20 nm colloidal silica. While the three samples prepared within each mount have different compositions, and thus different polishing rates, each mount was polished such that the hardest samples in the mount were sufficiently polished by the end. We mechanically tested the samples using the Vickers indentation method according to ASTM standard E92. At least three indents at 500 grams were performed on each sample. In some cases, we observed extensive cracking at 500 grams indent load; for such samples, the indent load was reduced to 300 grams. Indents with excessive cracking or deformation were excluded according to the standard.

We note here that we did not heat-treat the samples after melting and all characterization was done was as cast alloys. This might result in the alloy not being homogenized and having multiple phases. However, as shown in Sec. **??**, the dataset that we used for training (Borg et al. (2020)) has most alloys reported as cast without heat treatment. Our decision to not heat-treat the samples keeps the training and recommended datasets consistent with each other. Finally, we perform X-ray diffraction (XRD) on the samples to confirm phase formation and compare experimental patterns to predicted structures.

3 RESULTS

3.1 PAL 2.0 RECOMMENDATIONS FOR MANUFACTURING

The closed-loop PAL 2.0 materials discovery framework involves a "human-in-the-loop" approach that leverages domain expertise to impose constraints, create an initial physics-based hypothesis for the input space, and down-select final candidates to manufacture. Here, the constraints include exploring only those elements that can be manufactured in the arc-melting facility and have low cost.

We start by creating a physical descriptor search space for MPEAs, based on the elemental properties listed in Table 1. These properties are selected based on domain expertise. The first elemental property we consider is the valence electron count. This is a crucial property to include because it directly influences the bonding behavior, phase stability, and mechanical properties of the alloy. A recent study by Islam *et al.* (Islam et al. (2018)) further corroborates the importance of valence electron count in determination of the phase of MPEAs. We also consider three types of atomic radii, as listed in Table 1. The empirical atomic radius influences atomic packing and lattice distortion among other properties. In MPEAs, atoms of different elements have varying atomic radii, leading to a mismatch in atomic size. This size difference causes lattice distortion, which can strengthen the alloy through mechanisms such as solid-solution strengthening. Therefore, we include the empirical atomic radii in our surrogate model for hardness of the MPEAs. Similarly, the van der Waals atomic radius and covalent atomic radius are good indicators of weak bonding forces and interface behaviors and covalent bonding nature of the elements. Covalent bonds are directional and typically stronger than metallic bonds, so incorporating elements with strong covalent bonding tendencies can enhance the strength and hardness of an MPEA. Knowing the covalent atomic radius helps predict how these atoms will bond with surrounding metallic atoms and how much strengthening can occur. Lastly, we use the element's electron density. Data for the elemental properties is gathered using a combination of `www.webelements.com` database and Refs. Slater (1964); Cordero et al. (2008); pub (2023). A compiled list of the properties is available as part of the public GitHub repository that is mentioned in the Data and Code Availability statement.

We perform feature selection using LASSO (Tibshirani (1996)), and XGBoost (Chen & Guestrin (2016)) on the properties listed in Table 1 on the dataset curated by Borg *et al.* (Borg et al. (2020)). This step is vital as the goal is to enable PAL 2.0 to facilitate material discovery in a physics-

	Physio-chemical elemental property
1.	Valence electron count (VEC)
2.	Empirical atomic radius (r_{emp}) [pm]
3.	Van der Waals atomic radius (r_W) [pm]
4.	Covalent atomic radius (r_{cov}) [pm]
5.	Electron density ($\rho(r)$) [g/cm^3]

Table 1: Elemental property inputs to the PAL 2.0 framework. Data for the elemental properties is gathered from a combination of `www.webelements.com` database web (2023) and Refs. Slater (1964); Cordero et al. (2008); pub (2023).

driven manner, with the chosen properties establishing that link. We use mole fraction weighted elemental properties as inputs for LASSO and XGBoost. LASSO and XGBoost picked out all five properties, albeit with varying importance, as shown in Fig. 9 in the Appendix. This implies that all the properties we chose initially were important to predict hardness. As a result, we kept all five properties to build our input space for the GP models. It should be noted here that, due to limited availability of microstructural features such as the phase of the MPEAs, we do not include them in our models. However, adding microstructural data to the models would be valuable in future investigations.

To train the GP models, we used the 356 MPEAs from Borg *et al.* (Borg et al. (2020)) that have measured hardness values. The prediction accuracy of the two surrogate models we used (GP-0 and GP-NN) was assessed on a test dataset (10% of 356 MPEAs) using the mean squared error (MSE) loss. Both GP models exhibited similar performance with respect to the MSE loss, as shown in the Supplementary Information (SI) Fig. 10. Finally, the trained models were run to generate recommendations for manufacturing and testing them for hardness. The results of our recommendations are shown in Fig. 3 and discussed further in Sec. 3.3.

3.2 Generation of novel alloy compositions

For the first two manufacturing cycles, we used PAL 2.0 to explore the MPEAs in Borg et al. (2020) that did not have measured hardness values. After two cycles of identifying candidates and manufacturing, we expanded our compositional search space by generating new MPEAs based on the k-means clusters shown in Fig. 2. Section 2.2 provides details on k-means clustering for the MPEA dataset. Performing k-means clustering with two clusters on the known MPEA element compositions from Ref. Borg et al. (2020) allowed us to obtain two centroids representing the respective mean compositions of the clusters.

As shown in Fig. 2a, there was fairly little elemental overlap between the two centroids. The prominent elements of cluster 0 included Mo, Nb, Ta, Ti, and Zr, whereas cluster 1 was high in Al, Co, Cr, Fe, and Ni. Figure 2b shows that cluster 0 had a relatively large proportion of samples with hardness between 400 and 600; those in cluster 1 were more evenly distributed.

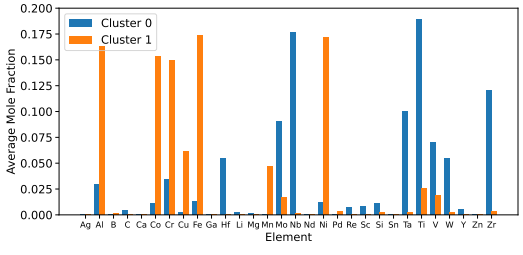

(a) Average mole fractions of elements in each cluster.

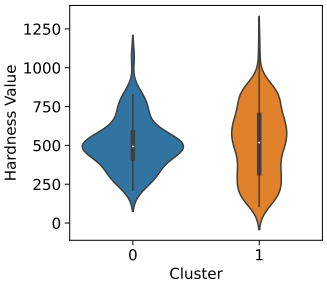

(b) Violin plot showing the distribution of hardness values for each of the two MPEA clusters.

Figure 2: Analysis of the MPEA dataset from Ref. 8 used in training the PAL 2.0 surrogate models to initiate the closed-loop materials discovery process.

Using the k-means clusters information, each novel MPEA composition is generated using Algorithm 1. Using this algorithm, we generated a dataset of 1000 novel alloys, of which 225 belonged to cluster 0 and 775 belonged to cluster 1. This split was chosen to reflect the distribution of MPEAs in the training data set (Ref. 8). We enforced physics-based composition generation by using cluster information from known alloys in Borg et al. (2020). The code used to generate the MPEA compositions and the generated list is provided in the public GitHub repository whose link is given in the Data and Code Availability section. Figure 8 shows the average mole fraction of each element in each cluster for the generated MPEA compositions.

Algorithm 1 Alloy composition generation algorithm using k-means clustering

Require: Observed alloy compositions, $m_{min} = 0.1$, $m_{max} = 0.35$
1: Perform k-means clustering
2: Identify important elements using centroid mole fraction $n_e > 0.01$.
3: Select N important elements, where N is chosen randomly from $3, 4, 5, 6, 7$
4: Select a random scale factor, $\mathcal{S}$, from $0.67 - 1.5$
5: Element mole fraction, $m_e = n_e \times \mathcal{S}$
6: Normalize m_e such that $\sum_e m_e = 1$.
7: **repeat**
8: max(m_e) * 0.9
9: Normalize m_e such that $\sum_e m_e = 1$.
10: **until** All m_e satisfy $m_{min} < m_e < m_{max}$
11: **return** Novel alloy composition

3.3 Synthesis and Testing of MPEAs

A total of 20 samples were fabricated over three closed-loop cycles based on the recommendations provided by PAL 2.0. We recommend MPEA candidates from Ref. Borg et al. (2020) for the first two rounds of manufacturing. In the third round of manufacturing, recommendations were made from the dataset generated in Sec. 3.2 (Fig. 8). We prioritized samples for synthesis based on the availability of elements and perceived manufacturability using arc-melting. During the third round

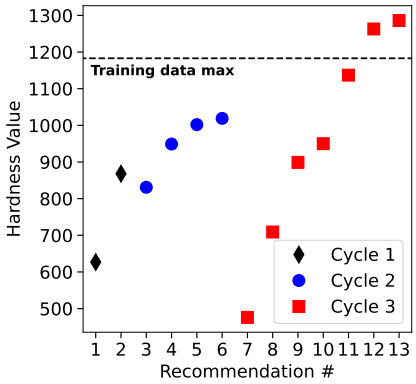

Figure 3: Experimentally measured hardness values of MPEA candidates recommended by PAL 2.0 over the course of three manufacturing cycles. The third cycle (red squares) represents novel alloy compositions generated in this work using the algorithm described in Sec. 3.2.

of manufacturing, some of the samples lost significant mass during synthesis, particularly samples that contained a mixture of light elements (aluminum and manganese) with refractory elements (Mo and W). This is expected given that aluminum boils at 2,470°C, whereas tungsten remains solid even at temperatures above 3,000°C. Given that the final composition of such samples is unknown, we did not test them for hardness. In the future, alloying strategies can be used to mitigate these losses, but such investigations are outside the scope of this paper.

We chose to test a total of seven samples based on how close the final mass was to the target mass. We performed between three and five indents on each sample at either 300 or 500 grams of indent force.

However, some of the very high hardness samples experienced brittle cracking during indentation that can be mitigated in the future by decreasing the indentation load. The measured and predicted hardness values from these tests are compared in Tables 3 and 2. We note here that the predictions of PAL 2.0 are within 20% of the measured hardness value. We expect these errors to exist since we do not consider descriptors for which we do not have data. This includes descriptors such as phases, grain size and other microstructural properties that are indicators of strengthening mechanisms in MPEAs.

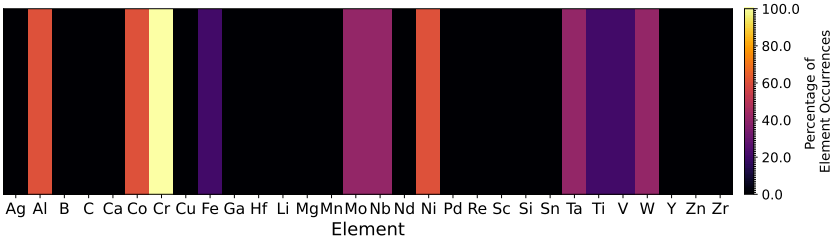

(a) Heat map of elements in MPEA compositions with hardness values above 900 in Ref. 8.

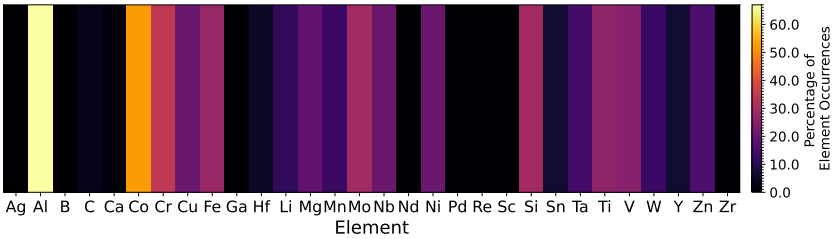

(b) Heat map of elements in MPEA compositions recommended by PAL 2.0.

Figure 4: Analysis of MPEA compositions (a) in the training dataset from Ref. 8 with hardness more than 900 and (b) recommended for manufacturing by PAL 2.0.

The measured hardness values from the three rounds of manufacturing are shown in Fig. 3. We see that PAL 2.0 consistently improves the hardness of the recommended MPEAs by at least 15% each round. Moreover, in the third round of manufacturing, we were able to identify two alloys with hardness values of 1263 and 1269. These values are 7% higher than the highest hardness value (1183) of any alloy in the initial training dataset (Borg et al. (2020)). In Fig. 4, we compare the elemental occurrence in PAL 2.0 recommendations versus alloys that have hardness values of more than 900 in the training dataset (Borg et al. (2020)). We see that, although chromium is present in every alloy with high hardness in the training dataset (Fig. 4a), our PAL recommendations give more weight to cobalt. We make another striking observation: The highest hardness materials recommended by PAL 2.0 incorporate silicon, which is not present in Fig. 4a. Moreover, these alloys were composed of cobalt, silicon and tantalum. This combination of elements is not present in a single alloy within the training dataset. This discovery shows the potential of PAL 2.0 to identify out-of-distribution materials with exceptional properties. It also demonstrates the value of physics-based models and closed-loop approaches to search parameter spaces beyond our chemical intuition.

We also carried out extensive characterization of the top performing alloys using SEM imaging and EDS mapping, XRD and analysis of the phase diagram using ThermoCalc. These results are shown in Figs. 5 and 12.

ThermoCalc modeling, applied to the Ta–Co–Si system, suggested the formation of a complex multiphase mixture including the CoSi B20 phase, a C14 Laves phase with a nominal composition of (Co,Si)Ta_2, and a Ta_5Si_3 DBL phase, Fig. 5b. These predictions aligned well with our experimental results. XRD revealed reflections consistent with Ta_5Si_3 and binary silicide phases, such as $TaCo_{16}Si_7$ and TaCoSi, confirming that the synthesis produced the predicted compound. Some oxidation was evident, indicated by the presence of CoO and SiO_2 in the XRD pattern, likely surface oxides. Figure 5a displays backscatter electron imaging and EDS maps showing two distinct phases: a nearly stoichiometric primary phase and a secondary phase enriched in Ta and depleted in

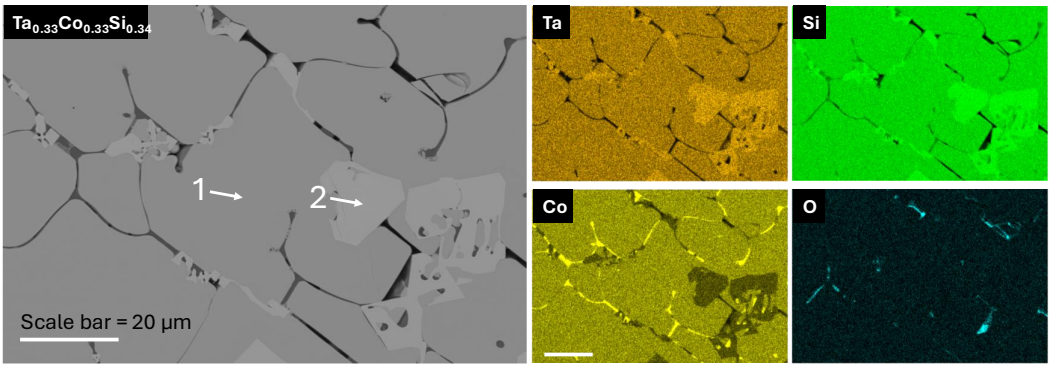

(a) Secondary electron image that shows two primary phases and EDS color maps showing the location of elements in the image.

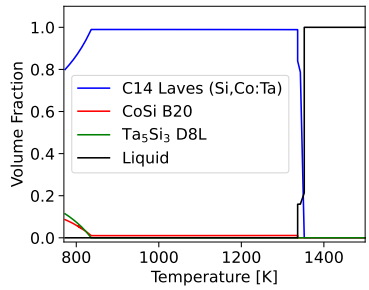

(b) Volume fractions of phases calculated using ThermoCalc.

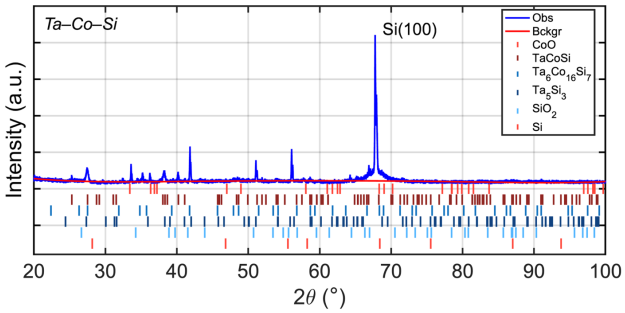

(c) XRD pattern.

Figure 5: Analysis of sample 53, $Co_{0.329}Si_{0.34}Ta_{0.33}$. (a) Secondary electron image that shows two primary phases and EDS color maps showing the location of elements in the image. Phases 1 and 2 marked in the figure are detailed in Table 4. (b) Volume fractions of different phases present as calculated using ThermoCalc, and (c) X-ray diffraction pattern for the $Co_{0.329}Si_{0.34}Ta_{0.33}$ system.

Co. The presence of cobalt enrichment along grain boundaries, as shown in the Co EDS maps, and fine intergranular cracking suggests residual thermal stress or phase mismatch, but confirms chemical partitioning consistent with ThermoCalc predictions. Taken together, these findings confirm that our PAL-guided selection and synthesis of TaCoSi yields multiphase structures, including relatively unexplored Ta–Co–Si silicides.

4 Conclusions

We have demonstrated that the PAL 2.0 model is capable of identifying superior high-hardness materials in the MPEA design space. Through just three rounds of predictions, the hardness values for the PAL-recommended and experimentally synthesized materials have increased significantly, being 7% above the highest previously existing hardness value in the 300-strong database. Through our closed-loop approach, we discovered multiple materials that had Vickers hardness values (VHN) above 1200 VHN, exceeding anything in the initial training data set. In addition, we were able to discover five new alloys with a hardness above 1000 VHN, in contrast to just three such alloys in the original data set.

For future studies, we propose two approaches that can lead to more accurate synthesis of the predicted compositions. The first is to incorporate some of the physics behind manufacturability (*i.e.,* melting temperature) into the model; the second is to explore additional processing routes in the synthesis approach. Additionally, given that the model has predicted high-hardness materials that are relatively inexpensive, light, and straightforward to synthesize, effort should be taken to scale up the material from the small ingots used for discovery to a useful material system in an application like hard-coating for wear-resistance.

REFERENCES

Reference Module in Chemistry, Molecular Sciences and Chemical Engineering. Number pub.1109750643. 2014. URL https://app.dimensions.ai/details/publication/pub.1109750643.

Atomic radius in the periodic table of elements. *National Center for Biotechnology Information, PubChem, https://pubchem.ncbi.nlm.nih.gov/periodic-table/atomic-radius.*, 2023.

Webelements. *https://www.webelements.com*, 2023.

Cafer Acemi, Brent Vela, Eli Norris, William Trehern, Kadri Can Atli, Conner Cleek, Raymundo Arróyave, and Ibrahim Karaman. Multi-objective, multi-constraint high-throughput design, synthesis, and characterization of tungsten-containing refractory multi-principal element alloys. *Acta Materialia*, 281:120379, 2024.

Sk Md Ahnaf Akif Alvi, Jan Janssen, Danial Khatamsaz, Danny Perez, Douglas Allaire, and Raymundo Arróyave. Hierarchical Gaussian process-based Bayesian optimization for materials discovery in high entropy alloy spaces. *Acta Materialia*, 289:120908, 2025.

Nicholas H. Angello, David M. Friday, Changhyun Hwang, Seungjoo Yi, Austin H. Cheng, Tiara C. Torres-Flores, Edward R. Jira, Wesley Wang, Alán Aspuru-Guzik, Martin D. Burke, Charles M. Schroeder, Ying Diao, and Nicholas E. Jackson. Closed-loop transfer enables artificial intelligence to yield chemical knowledge. *Nature*, 633:351–358, 2024. doi: https://doi.org/10.1038/s41586-024-07892-1. URL https://www.nature.com/articles/s41586-024-07892-1.

Maximilian Balandat, Brian Karrer, Daniel R. Jiang, Samuel Daulton, Benjamin Letham, Andrew Gordon Wilson, and Eytan Bakshy. Botorch: A framework for efficient monte-carlo bayesian optimization. 2019. doi: 10.48550/ARXIV.1910.06403. URL https://arxiv.org/abs/1910.06403.

Christopher KH Borg, Carolina Frey, Jasper Moh, Tresa M Pollock, Stéphane Gorsse, Daniel B Miracle, Oleg N Senkov, Bryce Meredig, and James E Saal. Expanded dataset of mechanical properties and observed phases of multi-principal element alloys. *Scientific Data*, 7(1):430, 2020. doi: https://doi.org/10.1038/s41597-020-00768-9.

Brady L. Bresnahan and David L. Poerschke. High-throughput multi-principal element alloy exploration using a novel composition gradient sintering technique. *Metals*, 14:558, 2024. doi: https://doi.org/10.3390/met14050558. URL https://www.mdpi.com/2075-4701/14/5/558.

Abhinav Chandraker, Sampad Barik, Nichenametla Jai Sai, and Ankur Chauhan. Experimentally Validated and Empirically Compared Machine Learning Approach for Predicting Yield Strength of Additively Manufactured Multi-Principal Element Alloys from Co–Cr–Fe–Mn–Ni System. *Metallurgical and Materials Transactions A*, 56(2):571–586, 2025.

Tianqi Chen and Carlos Guestrin. Xgboost: A scalable tree boosting system. In *Proceedings of the 22^{nd} ACM SIGKDD International Conference on Knowledge Discovery and Data Mining*, pp. 785–794, 2016.

Beatriz Cordero, Verónica Gómez, Ana E Platero-Prats, Marc Revés, Jorge Echeverría, Eduard Cremades, Flavia Barragán, and Santiago Alvarez. Covalent radii revisited. *Dalton Transactions*, (21):2832–2838, 2008.

E.P. George, W.A. Curtin, and C.C. Tasan. High entropy alloys: A focused review of mechanical properties and deformation mechanisms. *Acta Materialia*, 188:435–474, 2020. ISSN 1359-6454. doi: https://doi.org/10.1016/j.actamat.2019.12.015. URL https://www.sciencedirect.com/science/article/pii/S1359645419308444.

Edwin Gienger, Justin Rokisky, Denise Yin, Elizabeth A Pogue, and Bianca Piloseno. A database of multi-principal element alloy phase-specific mechanical properties measured with nanoindentation. *Data in Brief*, 55:110719, 2024.

Ethan Halpren, Xue Yao, Zhi Wen Chen, and Chandra Veer Singh. Machine learning assisted design of bcc high entropy alloys for room temperature hydrogen storage. *Acta Materialia*, 270:119841, 2024. ISSN 1359-6454. doi: https://doi.org/10.1016/j.actamat.2024.119841. URL https://www.sciencedirect.com/science/article/pii/S1359645424001940.

Trevor Hastings, Mrinalini Mulukutla, Danial Khatamsaz, Daniel Salas, Wenle Xu, Daniel Lewis, Nicole Person, Matthew Skokan, Braden Miller, James Paramore, et al. Accelerated Multi-Objective Alloy Discovery through Efficient Bayesian Methods: Application to the FCC High Entropy Alloy Space. *Acta Materialia*, pp. 121173, 2025.

Henry C. Herbol, Weici Hu, Peter Frazier, Paulette Clancy, and Matthias Poloczek. Efficient search of compositional space for hybrid organic-inorganic perovskites via bayesian optimization. *npj Computational Materials*, 4(1):51, September 2018. ISSN 2057-3960. URL https://doi.org/10.1038/s41524-018-0106-7.

Henry C. Herbol, Matthias Poloczek, and Paulette Clancy. Cost-effective materials discovery: Bayesian optimization across multiple information sources. *Mater. Horiz.*, 7:2113–2123, 2020. doi: 10.1039/D0MH00062K. URL http://dx.doi.org/10.1039/D0MH00062K.

Shuo Huang, Erik Holmström, Olle Eriksson, and Levente Vitos. Mapping the magnetic transition temperatures for medium- and high-entropy alloys. *Intermetallics*, 95:80–84, 2018. ISSN 0966-9795. doi: https://doi.org/10.1016/j.intermet.2018.01.016. URL https://www.sciencedirect.com/science/article/pii/S0966979517311688.

Nusrat Islam, Wenjiang Huang, and Houlong L Zhuang. Machine learning for phase selection in multi-principal element alloys. *Computational Materials Science*, 150:230–235, 2018. doi: https://doi.org/10.1016/j.commatsci.2018.04.003.

Lance Kavalsky, Vinay I. Hegde, Eric Muckley, Matthew S. Johnson, Bryce Meredig, and Venkatasubramanian Viswanathan. By how much can closed-loop frameworks accelerate computational materials discovery? *Digital Discovery*, 2:1112–1125, 2023. doi: 10.1039/D2DD00133K. URL http://dx.doi.org/10.1039/D2DD00133K.

Danial Khatamsaz, Brent Vela, Prashant Singh, Duane D Johnson, Douglas Allaire, and Raymundo Arróyave. Bayesian optimization with active learning of design constraints using an entropy-based approach. *npj Computational Materials*, 9(1):49, 2023.

Diederik P Kingma and Jimmy Ba. Adam: A method for stochastic optimization. *arXiv preprint arXiv:1412.6980*, 2014.

Shalini Roy Koneru, Kamalnath Kadirvel, and Yunzhi Wang. High-throughput design of multi-principal element alloys with spinodal decomposition assisted microstructures. *Journal of Phase Equilibria and Diffusion*, 43:753–763, 2022. doi: https://doi.org/10.1007/s11669-022-00977-2. URL https://link.springer.com/article/10.1007/s11669-022-00977-2.

A. Gilad Kusne, Heshan Yu, Changming Wu, Huairuo Zhang, Jason Hattrick-Simpers, Brian DeCost, Suchismita Sarker, Corey Oses, Cormac Toher, Stefano Curtarolo, Albert V. Davydov, Ritesh Agarwal, Leonid A. Bendersky, Mo Li, Apurva Mehta, and Ichiro Takeuchi. On-the-fly closed-loop materials discovery via bayesian active learning. *Nature Communications*, 2020. doi: 10.1038/s41467-020-19597-w. URL https://www.nature.com/articles/s41467-020-19597-w.

F. Körmann, D. Ma, D. D. Belyea, M. S. Lucas, C. W. Miller, B. Grabowski, and M. H. F. Sluiter. "Treasure maps" for magnetic high-entropy-alloys from theory and experiment. *Applied Physics Letters*, 107(14):142404, 10 2015. ISSN 0003-6951. doi: 10.1063/1.4932571. URL https://doi.org/10.1063/1.4932571.

Chenze Li, Michael Ferry, Jamie J Kruzic, and Xiaopeng Li. Review: Multi-principal element alloys by additive manufacturing. *Journal of Materials Science*, 57:9903–9935, 2022. doi: https://doi.org/10.1007/s10853-022-06961-y. URL https://link.springer.com/article/10.1007/s10853-022-06961-y.

Z. Li, S. Li, and N. Birbilis. A machine learning-driven framework for the property prediction and generative design of multiple principal element alloys. *Materials Today Communications*, 38:107940, 2024. ISSN 2352-4928. doi: https://doi.org/10.1016/j.mtcomm.2023.107940. URL https://www.sciencedirect.com/science/article/pii/S2352492823026314.

Xianglin Liu, Jiaxin Zhang, and Zongrui Pei. Machine learning for high-entropy alloys: Progress, challenges and opportunities. *Progress in Materials Science*, 2022. URL https://api.semanticscholar.org/CorpusID:252110722.

Mrinalini Mulukutla, Robert Robinson, Danial Khatamsaz, Brent Vela, Trevor Hastings, Nhu Vu, and Raymundo Arróyave. Supply risk-aware alloy discovery and design: A case study on the monbtivw system. *Materialia*, 39:102332, 2025.

Ahmad Ostovari Moghaddam, Nataliya A. Shaburova, Marina N. Samodurova, Amin Abdollahzadeh, and Evgeny A. Trofimov. Additive manufacturing of high entropy alloys: A practical review. *Journal of Materials Science & Technology*, 77:131–162, 2021. ISSN 1005-0302. doi: https://doi.org/10.1016/j.jmst.2020.11.029. URL https://www.sciencedirect.com/science/article/pii/S1005030220309476.

James D. Paramore, Trevor Hastings, Brady G. Butler, Michael T. Hurst, Daniel O. Lewis, Eli Norris, Benjamin Barkai, Joshua Cline, Braden Miller, Jose Cortes, Ibrahim Karaman, George M. Pharr, and Raymundo Arróyave. Two-shot optimization of compositionally complex refractory alloys. *Acta Materialia*, 289:120820, 2025. ISSN 1359-6454. doi: https://doi.org/10.1016/j.actamat.2025.120820. URL https://www.sciencedirect.com/science/article/pii/S1359645425001120.

Jonathan W. Pegues, Michael A. Melia, Raymond Puckett, Shaun R. Whetten, Nicolas Argibay, and Andrew B. Kustas. Exploring additive manufacturing as a high-throughput screening tool for multiphase high entropy alloys. *Additive Manufacturing*, 37:101598, 2021. ISSN 2214-8604. doi: https://doi.org/10.1016/j.addma.2020.101598. URL https://www.sciencedirect.com/science/article/pii/S2214860420309702.

Elizabeth A. Pogue, Alexander New, Kyle McElroy, Nam Q. Le, Michael J. Pekala, Ian McCue, Eddie Gienger, Janna Domenico, Elizabeth Hedrick, Tyrel M. McQueen, Brandon Wilfong, Christine D. Piatko, Christopher R. Ratto, Andrew Lennon, Christine Chung, Timothy Montalbano, Gregory Bassen, and Christopher D. Stiles. Closed-loop superconducting materials discovery. *npj Computaitonal Materials*, 2023. doi: 10.1038/s41524-023-01131-3. URL https://www.nature.com/articles/s41524-023-01131-3.

Ziyuan Rao, Dirk Ponge, Fritz Körmann, Yuji Ikeda, Oldřich Schneeweiss, Martin Friák, Jörg Neugebauer, Dierk Raabe, and Zhiming Li. Invar effects in fenico medium entropy alloys: From an invar treasure map to alloy design. *Intermetallics*, 111:106520, 2019. ISSN 0966-9795. doi: https://doi.org/10.1016/j.intermet.2019.106520. URL https://www.sciencedirect.com/science/article/pii/S0966979519303449.

Ziyuan Rao, Hauke Springer, Dirk Ponge, and Zhiming Li. Combinatorial development of multicomponent invar alloys via rapid alloy prototyping. *Materialia*, 21:101326, 2022a. ISSN 2589-1529. doi: https://doi.org/10.1016/j.mtla.2022.101326. URL https://www.sciencedirect.com/science/article/pii/S2589152922000138.

Ziyuan Rao, Po-Yen Tung, Ruiwen Xie, Ye Wei, Hongbin Zhang, Alberto Ferrari, T.P.C. Klaver, Fritz Körmann, Prithiv Thoudden Sukumar, Alisson Kwiatkowski da Silva, Yao Chen, Zhiming Li, Dirk Ponge, Jörg Neugebauer, Oliver Gutfleisch, Stefan Bauer, and Dierk Raabe. Machine learning–enabled high-entropy alloy discovery. *Science*, 378(6615):78–85, 2022b. doi: 10.1126/science.abo4940. URL https://www.science.org/doi/abs/10.1126/science.abo4940.

Ankit Roy, Aqmar Hussain, Prince Sharma, Ganesh Balasubramanian, M.F.N. Taufique, Ram Devanathan, Prashant Singh, and Duane D. Johnson. Rapid discovery of high hardness multi-principal-element alloys using a generative adversarial network model. *Acta Materialia*, 257:119177, 2023. ISSN 1359-6454. doi: https://doi.org/10.1016/j.actamat.

2023.119177. URL https://www.sciencedirect.com/science/article/pii/S1359645423005086.

Nichenametla Jai Sai, Punit Rathore, and Ankur Chauhan. Machine learning-based predictions of fatigue life for multi-principal element alloys. *Scripta Materialia*, 226:115214, 2023.

Maitreyee Sharma Priyadarshini, Oluwaseun Romiluyi, Yiran Wang, Kumar Miskin, Connor Ganley, and Paulette Clancy. PAL 2.0: A physics-driven bayesian optimization framework for material discovery. *Materials Horizons*, 11(3):781–791, 2024.

John C Slater. Atomic radii in crystals. *The Journal of Chemical Physics*, 41(10):3199–3204, 1964.

Jasper Snoek, Hugo Larochelle, and Ryan P Adams. Practical bayesian optimization of machine learning algorithms. In F. Pereira, C. J. C. Burges, L. Bottou, and K. Q. Weinberger (eds.), *Advances in Neural Information Processing Systems*, volume 25. Curran Associates, Inc., 2012. URL https://proceedings.neurips.cc/paper/2012/file/05311655a15b75fab86956663e1819cd-Paper.pdf.

Felix Strieth-Kalthoff, Han Hao, Vandana Rathore, Joshua Derasp, Théophile Gaudin, Nicholas H. Angello, Martin Seifrid, Ekaterina Trushina, Mason Guy, Junliang Liu, Xun Tang, Masashi Mamada, Wesley Wang, Tuul Tsagaantsooj, Cyrille Lavigne, Robert Pollice, Tony C. Wu, Kazuhiro Hotta, Leticia Bodo, Shangyu Li, Mohammad Haddadnia, Agnieszka Wołos, Rafał Roszak, Cher Tian Ser, Carlota Bozal-Ginesta, Riley J. Hickman, Jenya Vestfrid, Andrés Aguilar-Granda, Elena L. Klimareva, Ralph C. Sigerson, Wenduan Hou, Daniel Gahler, Slawomir Lach, Adrian Warzybok, Oleg Borodin, Simon Rohrbach, Benjamin Sanchez-Lengeling, Chihaya Adachi, Bartosz A. Grzybowski, Leroy Cronin, Jason E. Hein, Martin D. Burke, and Alán Aspuru-Guzik. Delocalized, asynchronous, closed-loop discovery of organic laser emitters. *Science*, 384(6697): eadk9227, 2024. doi: 10.1126/science.adk9227. URL https://www.science.org/doi/abs/10.1126/science.adk9227.

Gloria A Sulley, Jonathan Raush, Matthew M Montemore, and Jihun Hamm. Accelerating high-entropy alloy discovery: efficient exploration via active learning. *Scripta Materialia*, 249:116180, 2024. ISSN 1359-6462. doi: https://doi.org/10.1016/j.scriptamat.2024.116180. URL https://www.sciencedirect.com/science/article/pii/S135964622400215X.

Robert Tibshirani. Regression shrinkage and selection via the lasso. *Journal of the Royal Statistical Society Series B: Statistical Methodology*, 58(1):267–288, 1996.

Duo Wang, Lei Liu, Wenjiang Huang, and Houlong L Zhuang. Semiconducting SiGeSn high-entropy alloy: A density functional theory study. *Journal of Applied Physics*, 126(22), 2019.

J.-W. Yeh, S.-K. Chen, S.-J. Lin, J.-Y. Gan, T.-S. Chin, T.-T. Shun, C.-H. Tsau, and S.-Y. Chang. Nanostructured high-entropy alloys with multiple principal elements: Novel alloy design concepts and outcomes. *Advanced Engineering Materials*, 6(5):299–303, 2004. doi: https://doi.org/10.1002/adem.200300567. URL https://onlinelibrary.wiley.com/doi/abs/10.1002/adem.200300567.

A APPENDIX: K-MEANS CLUSTERING RESULTS

In this section, we show an analysis of the the inertia score and mean silhouette score to guide the choice of optimal number of clusters in k-means clustering. We also show the distribution of new MPEA compositions generated using the generated clusters.

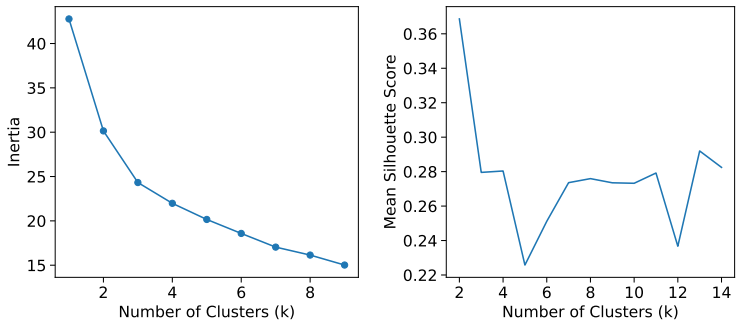

(a) Inertia Score (b) Mean silhouette score

Figure 6: Two scoring metrics used for different k-means cluster sizes to determine the optimal number of clusters in the MPEA dataset Ref.Borg et al. (2020): (a) the inertia score, (b) mean silhouette score.

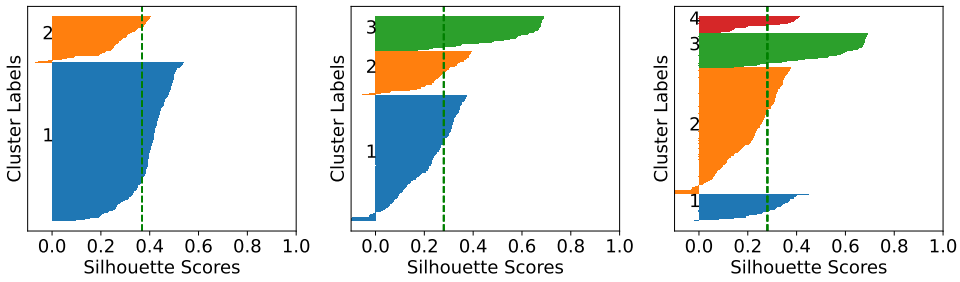

(a) k = 2 (b) k = 3 (c) k = 4

Figure 7: Silhouette score distributions for varying cluster sizes between 2 and 4, using k-means clustering for the MPEA dataset.Borg et al. (2020).

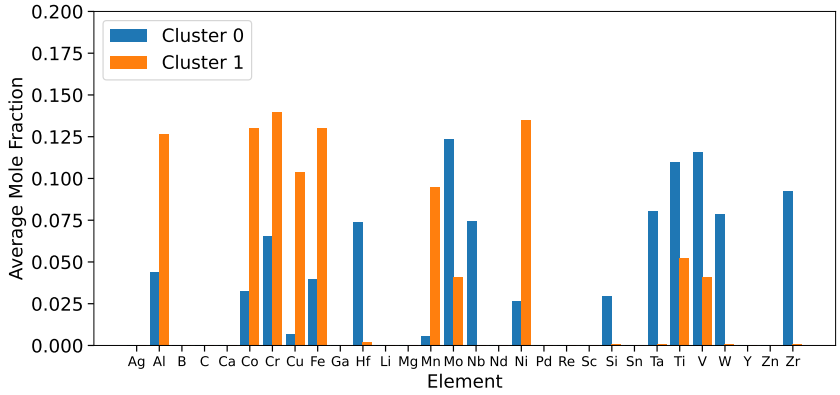

Figure 8: Analysis of the MPEA dataset created using the alloy generation algorithm. The figure shows average mole fractions of elements in each cluster for the generated MPEA compositions.

B Appendix: Feature seleciton and PAL 2.0 surrogate models training results

Figure 9 shows the property importance for predicting the hardness of MPEAs using LASSO and XGBoost.

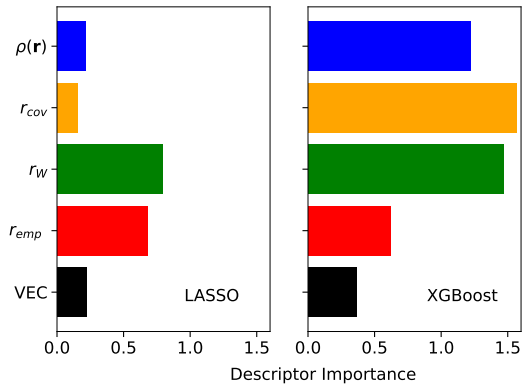

Figure 9: Descriptor importance values using LASSO Tibshirani (1996) (left) and XGBoost Chen & Guestrin (2016) (right).

Here, we also compare the predictive accuracy of three surrogate models that are part of the PAL 2.0 Bayesian optimization framework - Gaussian process with a zero prior (GP-0), Gaussian process with a linear prior (GP-L) and Gaussian process with a neural network prior (GP-NN). The violin plots are generated by creating 25 different train-test data splits from the Borg *et al.* dataset Borg et al. (2020) using the bagging methodology. We use 90% of the data for training and 10% of the data for testing. Our comparison shows that all three surrogate models perform nearly the same, with the GP-NN model having slightly lower overall error. Based on our analysis, we use these surrogate models in the PAL 2.0 framework to generate recommendations for manufacturing and then used an equal weight consensus scheme to give recommendations to the experimental team. Details on the three surrogate models can be found in our previous publication on PAL 2.0. Sharma Priyadarshini et al. (2024)

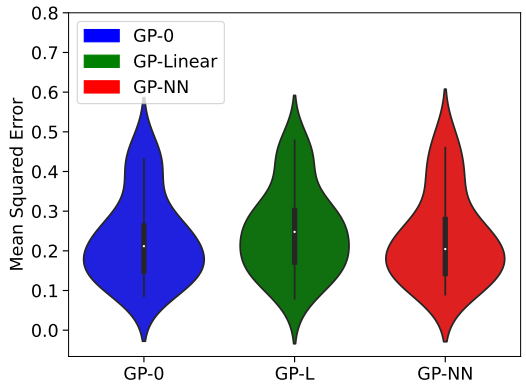

Figure 10: Predictive accuracy of GP-0, GP-L and GP-NN models on the MPEA dataset from Borg *et al.* (Borg et al. (2020)).

C Appendix: Experimental results analysis

In this section, we list the hardness value measurements taken from the three rounds of manufacturing and share experimental results from SEM and EDS characterization of the two top performing

alloys discovered. We also present a phase analysis from the Thermocalc software for these alloys at the end of this section.

Sample # and Elemental Composition	Force (g)	Measured VHN	Predicted VHN
27 $Al_{0.167}Co_{0.167}Cr_{0.167}Fe_{0.167}Ni_{0.167}Si_{0.167}$	300	868	733
254 $Co_{0.111}Cu_{0.111}Fe_{0.111}Nb_{0.556}Ni_{0.111}$	500	627	763
19 $Al_{0.174}Co_{0.174}Cr_{0.174}Fe_{0.174}Nb_{0.13}Ni_{0.174}$	300	831	781
93 $Co_{0.25}Cr_{0.25}Mo_{0.25}Nb_{0.25}$	300	1019	719.5
228 $Al_{0.25}Cr_{0.25}Mo_{0.25}Nb_{0.25}$	300	1002	691.2
34 $Al_{0.147}Co_{0.147}Cr_{0.147}Cu_{0.147}Ni_{0.147}Ti_{0.147}Y_{0.118}$	300	949	666.4

Table 2: Measured and predicted Vickers hardness values (VHN) for synthesized materials from the first two rounds of manufacturing.

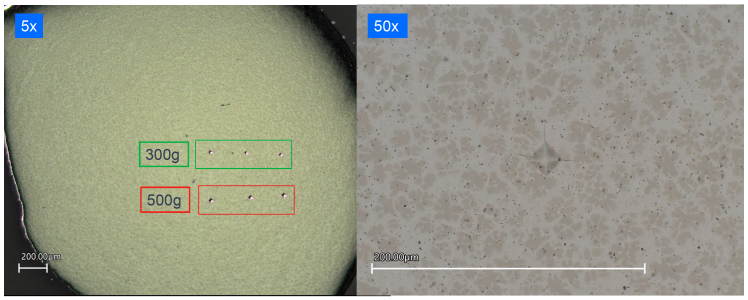

Figure 11: Indentation and microstructure of sample 27 from Table 2 ($Al_{0.167}Co_{0.167}Cr_{0.167}Fe_{0.167}Ni_{0.167}Si_{0.167}$). The indents made at 300 g force are used for hardness measurements.

C.0.1 Materials Characterization of the Fe–Mo–Si system

ThermoCalc predicted equilibrium phases for the Fe–Mo–Si system included Mo_5Si_3 and FeSi (BCC) in near-equimolar proportions, along with some residual Mo, Fig. 12. SEM imaging and EDS mapping showed a dominant, nearly equiatomic FeMoSi phase. Preliminary XRD-indexing identified the presence of a metallic iron based BCC phase, Fig. 12. Fe_2Si and Mo_3Si are also present in the material. Given that the EDS maps show a roughly equiatomic FeMoSi phase, there is likely a solid solution of these silicides that approaches an FeMoSi composition. Previous studies not included in our training data show this material class to be exceptionally high hardness. A secondary phase is enriched in Fe with some Mo depletion. It is possibly the thermodynamically predicted BCC phase (Fig. 12) with some Mo substitutions. A third, oxidized phase was also detected, likely forming due to air exposure, as suggested by oxygen-rich regions in EDS, and confirmed with FeO reflections identified in XRD. The coexistence of these phases reinforces the concept that this alloy lies in a largely unexplored compositional space where conventional ternary phase diagrams offer limited guidance.

Figure 12b shows that two binary phases are present in the $Fe_{0.34}Mo_{0.347}Si_{0.312}$ alloy, BCC B2 phase with Fe:Si present in a 1:1 ratio with some Mo impurities in the lattice. A second binary phase with chemical formula of Mo_5Si_3 and the D8m crystal structure dominates the volume fraction of the alloy.

Sample # and Elemental Composition	Indent	Force (g)	Measured VHN	Predicted VHN
42	1	300	1185	
	2	300	1101	
$Co_{0.34}Si_{0.333}Ta_{0.327}$	3	300	1093	
	4	300	1175	
	Average	300	1137	931
53	1	500	1170	
	2	500	1245	
$Co_{0.329}Si_{0.34}Ta_{0.33}$	3	500	1363	
	4	500	1309	
	Average	500	1269	894
72	1	300	880	
	2	300	992	
$Fe_{0.213}Si_{0.11}V_{0.35}W_{0.327}$	3	300	872	
	4	300	864	
	Average	300	900	862
114	1	500	974	
	2	500	952	
$Co_{0.311}Fe_{0.345}Si_{0.344}$	3	500	940	
	4	500	933	
	Average	500	950	894
118	1	300	750	
	2	300	728	
$Al_{0.342}Fe_{0.315}Mo_{0.343}$	3	300	711	
	4	300	653	
	Average	300	709	1034
170	1	500	1297	
	2	500	1323	
$Fe_{0.34}Mo_{0.347}Si_{0.312}$	3	500	1387	
	4	500	1081	
	Average	500	1263	1042
489	1	300	475	
	2	300	479	
$Al_{0.331}Co_{0.347}V_{0.322}$	3	300	455	
	4	300	494	
	Average	300	476	839

Table 3: Measured and predicted Vickers hardness values (VHN) for synthesized materials with novel compositions recommended based on the dataset generated using the method discussed in Sec. 3.2. Results from the first two rounds of manufacturing are listed in Table 2.

Phase	Ta (at%)	Co (at%)	Si (at%)	0 (at%)
1	31	30	38	1
2	42	17	38	3

Table 4: Phase composition of phase 1 and 2 in the sample 53, $Co_{0.329}Si_{0.34}Ta_{0.33}$. Phase 1 and 2 are shown in Fig. 5a

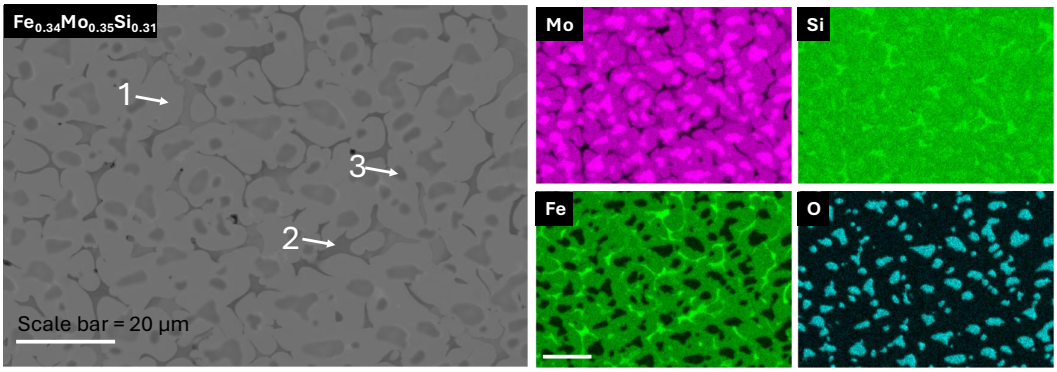

(a)

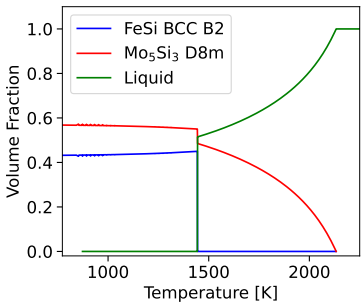

(b)

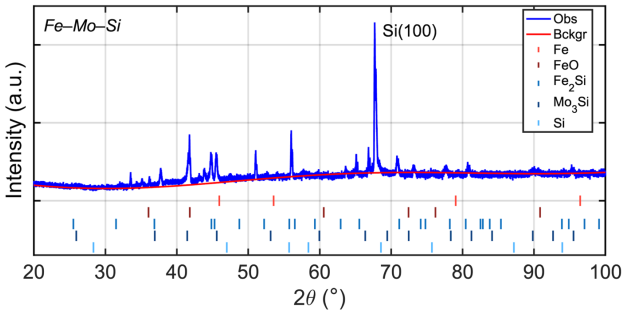

(c)

Figure 12: Analysis of sample 170, $Fe_{0.34}Mo_{0.347}Si_{0.312}$, (a) Secondary electron image that shows three primary phases and EDS color maps showing the location of elements in the image. The phase composition for each phase is given in Table 5, (b) Volume fractions of different phases present as calculated using ThermoCalc, and (c) X-ray diffraction pattern for the $Fe_{0.34}Mo_{0.347}Si_{0.312}$ alloy.

Phase	Fe (at%)	Mo (at%)	Si (at%)	0 (at%)
1	36	31	29	4
2	58	8	33	1
3	7	24	17	52

Table 5: Phase composition of phase 1, 2 and 3 in sample 170, $Fe_{0.34}Mo_{0.347}Si_{0.312}$. Phases 1, 2 and 3 are shown in Fig. 12